Research Paper

Development and validation of a comprehensive dynamic mathematical model for hybrid PV/T solar collectors

Riccardo Simonetti, Luca Molinaroli*, Giampaolo Manzolini

Dipartimento di Energia, Politecnico di Milano, Via Lambruschini 4, 20156 Milano, Italy

In this paper, a model for the simulation of a hybrid photovoltaic-thermal collector under transient regime is developed and validated. The model is built using a control volume approach, the collector is divided into small elemental volumes where energy equation is solved using a bi-dimensional finite difference method. The model is validated against experimental data obtained from a two weeks testing in real environmental weather con-ditions on two hybrid PV/T solar tiles connected in series. An agreement between the experimental and nu-merical values of the instantaneous power production and the water outlet temperature within ± 4 W and within ± 0.5 K respectively is found. On a daily basis, the calculated electrical and thermal energies agree within

− 2.64% to +1.73% and within −4.90% to +7.37% with experimental data, allowing to state that the de-veloped model is quite a reliable tool both for short-term and long-term yield analysis at component or system level.

Keywords: Modelling, PV/T collector, Simulation, Testing

HIGHLIGHTS

- A comprehensive dynamic model for hybrid PV/T solar tiles.
- Power production and water outlet temperature are computed.
- Model is validated over data collected during a dedicated experimental campaign.
- Instantaneous data agree within ± 4 W and within ± 0.5 K.
- Daily basis electrical energy agrees within ± 3%, thermal energy within −5% to +8%.

1. Introduction

The hybrid photovoltaic/thermal (PV/T) solar collector integrates a PV module with a solar thermal collector simultaneously producing electric and thermal energy. In this way, a reduction of the PV cells temperature, which is beneficial for the electric conversion efficiency, and a simultaneous increase of coolant (air or water) temperature are achieved. Although the electrical and the thermal performance of PV/T collectors are lower than the ones of separate PV and conventional thermal collectors, the converted energy per unit surface area is usually than the one produced by one PV panel and one thermal collector next to each other and, therefore, the PV/T technology results strongly attractive for applications where the surface area availability is a constraint [1].

The development of both thermal and electric models and their coupling are necessary to accurately predict the performance of PV/T solar collectors. Different approaches are found in the scientific literature leading to various models, from simple to complex.

Zondag et al. [2] developed and validated a 3D dynamical model and three steady state (3D, 2D and 1D) models of a double-glazed PV/T collector. The electric modelling was based on the adoption of the power coefficient to correct the power production at different temperatures. Numerical data agreed with experimental ones within 5%.

Chow [3] developed a dynamic model for a single-glazed flat plate PV/T collector based on the control-volume approach. The influence of cell temperature on collector power production was accounted for using the typical power coefficient correction. The model was later updated and validated by Bhattarai et al. [4] through a comparison with experimental data finding that the maximum difference between the measured and predicted values was 1.17 K for water temperature at collector outlet, 2% for collector thermal efficiency and 0.2% for collector electrical efficiency.

Received 17 October 2017;
Received in revised form 15 January 2018;
Accepted 25 January 2018

* Corresponding author.
E-mail address: luca.molinaroli@polimi.it (L. Molinaroli).

Nomenclature

c	specific heat [J kg^{-1} K^{-1}]
D	diameter [m]
E	energy [J]
e	error [dimensionless]
e^-	electron charge [C]
E_G	bandgap energy of the silicon [eV]
F	view factor [dimensionless]
G	solar irradiance [W m^{-2}]
g	standard acceleration due to gravity [m s^{-2}]
Gr	Grashof number = $\frac{g\beta\cos(\theta)\Delta TL^3}{(\mu/\rho)^2}$ [dimensionless]
h	convective heat transfer coefficient [W m^{-2} K^{-1}]
I	current [A]
k	thermal conductivity [W m^{-1} K^{-1}]
k_B	Boltzmann constant [eV K^{-1}]
L	collector length [m]
M	mass [kg]
$\dot{m}$	mass flow rate [kg s^{-1}]
n	diode ideality factor [dimensionless]
Nu	Nusselt number = $\frac{hL}{k}$ [dimensionless]
p_{SAT}	saturated water vapour pressure [Pa]
Pr	Prandtl number = $\frac{\mu c_P}{k}$ [dimensionless]
$\dot{Q}$	heat flow rate [W]
$\dot{q}$	conduction heat flux per unit area [W m^{-2}]
R	thermal resistance [m^2 K W^{-1}]
Ra	Rayleigh number = $GrPr$ [dimensionless]
Re	Reynolds number = $\frac{\rho vL}{\mu}$ [dimensionless]
s	thickness [m]
T	temperature [K]
t	time [s]
U	internal energy [J kg^{-1}]
V	voltage [V]
v	velocity [m s^{-1}]
$\dot{W}$	power [W]
z	height [m]

Greek symbols

$\alpha_{I_{SC}}$	temperature coefficient for short circuit current [dimensionless]
α_O	absorbance [dimensionless]
β	isobaric thermal expansion coefficient [K^{-1}]
ε_O	emissivity [dimensionless]
η	fin efficiency [dimensionless]
θ	tilt angle [°]
μ	dynamic viscosity [Pa s]
ρ	density [kg m^{-3}]
ρ_O	reflectance [dimensionless]
σ	stefan-Boltzmann constant [dimensionless]
τ_O	transmittance [dimensionless]

Subscripts

AIR	air
A	absorber plate
DIF	diffuse
DP	dew point
D	diode
EL	electrical
EVA	EVA (Ethilen-Vinyl-Acetate) layer
EXP	experimental
FC	forced convection
F	forex layer (Back cover)
GND	ground
G	glass
	heat transfer fluid
H	horizontal
IF	insulating foam
IN	inner or inlet
MC	mixed convection
NC	natural convection
NUM	numerical
OUT	outer or outlet
PVC	photovoltaic cell
PV	photovoltaic layer
REF	reference conditions
SH	shunt
SKY	sky
SUN	sun
S	series
TA	thermal adhesive
TC	thermal contact
TD	tedlar
TH	thermal
T	tube
x	x direction
y	y direction

Amrizal et al. [5] developed a dynamic model of a flat plate PV/T collector based on the equation reported in EN 12975 [6] coupled with the single-diode photovoltaic model. The model required four parameters to simulate the dynamic operation of the PV/T collector calibrated against experimental data. Once calibrated, the model accuracy was satisfactory.

Touafek et al. [7] developed a dynamic model of a sheet-and-tube PV/T collector assuming an average value of the temperature for each layer and using the power coefficient relation between cell temperature and conversion efficiency to account for its influence on power production.

Khelifa et al. [8] developed and validated a dynamic model of a sheet-and-tube PV/T collector using a 2D control-volume approach. The influence of cell temperature on cell power production was accounted using the power coefficient relation. The model was validated using in-house experimental results finding that the root mean square of percentage deviations is equal to 2.66% for water outlet temperature and 16.17% for useful thermal energy.

Haurant et al. [9] developed and validated a 3D dynamic model for a sheet-and-tube PV/T collector. The Shockley single-diode approximation to describe the PV cell was implemented. The model was validated under steady state and transient conditions, showing a tendency to overestimate the collector power production with a maximum difference equal to 1.7 W in steady-state conditions and larger values in transient ones. Moreover, the fluid temperature at collector outlet was predicted within 0.2 K and 2 K during steady and transient conditions respectively.

Aste et al. [10] developed a dynamic model of an innovative roll-bond PV/T collector assuming a uniform temperature in each layer and using the power coefficient to correct the PV cell conversion efficiency. The model was validated against in-house experimental results finding a root mean square percentage deviations around 15% for the power production and around 4–5% for the water temperatures. Later this model was improved to simulate a commercial roll-bond PV/T collector [11]. After a calibration of the model parameter using a best fitting procedure, an agreement between the measured and model collector daily electrical energy and the water temperatures within 2.52% and within 0.27 K was respectively found.

Rejeb et al. [12] developed a dynamic model of a sheet-and-tube PV/T collector assuming a temperature variation in the coolant fluid direction only and using the power coefficient relationship to account for cell temperature influence on collector power production. The model was validate against literature data [4] finding that the root mean square percentage deviation of thermal efficiency and electrical efficiency were 0.575% and 2.31% respectively.

Guo et al. [13] developed a 1D dynamic model of a sheet-and-tube tri-functional PV/T collector assuming a 2D temperature distribution for the absorber plate only. The effect of cell temperature on conversion efficiency was modelled considering the power coefficient correction approach. The model was validated using previous results [14] finding a root mean square deviation for the power production of 18.7% in air-heating mode and of 15.8% in water-heating mode.

Guarracino et al. [15] developed a dynamic model suitable for unglazed, single glazed and double glazed sheet-and-tube PV/T collector. The model assumed constant temperature along the layer thickness but variable temperature along the layer plane. The influence of the cell temperature on conversion of solar radiation was modelled considering the power coefficient approach. The model was validated both in steady-state and in dynamic conditions against third party available data. An agreement within ± 8% for fluid temperature difference and thermal efficiency in steady-state conditions was found, whereas in dynamic condition the model was able to compute the time constant of the PV/T collector tested by Amrizal et al.'s [5] very closely.

Hazami et al. [16] carried out an experimental analysis of a PV/T collector under outdoor weather conditions. The results were then used to check the validity of TRNSYS Type 50a finding that its accuracy to predict the cell temperature and the power production within 4–5%.

Finally, Shi et al. [17] developed a 2D dynamic model of a natural circulation, sheet-and-tube PV/T collector to be integrated at building level. The model was validated against experimental results obtained with an indoor laboratory showing an accuracy around −4.6%.

As shown, the modelling PV/T collector technology has deserved a lot of attention over the last years. Although all the previous papers provide very valuable tools for PV/T collector simulation, the deviations between experimental and numerical values of the power production and of the water outlet temperature may be very large, especially in real, outdoor weather conditions. Consequently, the purpose of this paper is to develop and validate a comprehensive dynamic model of a hybrid, unglazed, sheet-and-tube PV/T solar collector improving the prediction capability with respect to models available in open literature both on instantaneous values of power production and water outlet temperature and on the daily values of electrical and thermal energy production and to find also its limitation.

Compared to previously published models, the one developed and described in the present paper: (i) considers all the layers and materials that are used to build the PV/T collector, (ii) uses the five parameters electric equivalent approach to account for PV power production introducing a more physical way to deal with PV cell connection in series, and (iii) introduces a new approach to account for the heat transfer between the tube and the coolant fluid. Moreover, differently from previously published papers, the validation of the model is carried out considering both "slow variation" and "steep variation" of working conditions and under clear sky and cloudy sky days. This allows to stress the model and put in evidence its limitations.

2. Model description

The model developed in this study refers to the hybrid PV/T solar collector shown in Fig. 1.

The hybrid PV/T solar collector is an unglazed, sheet-and-tube PV/T solar tile that consists of a glass, twenty-eight monocrystaline PV cells (EVA + amorphous silicon cell + EVA + Tedlar), an aluminium plate absorber glued to the Tedlar layer through a transparent thermal adhesive, one bended copper tubes soldered on the back of the aluminium plate, an insulating foam and a Forex frame. The overall dynamic model of the PV/T solar tile combines the thermal model and the electrical model described in Sections 2.1 and 2.2 respectively.

2.1. Thermal model

The developed thermal model is a 2D + 1D dynamic model in which each layer of the PV/T tile is divided into small elemental volumes, as shown in Fig. 2, and where the temperature varies only in the x–y plane (2D) whereas it is constant in the z direction (1D). The application of the unsteady energy equation to each elemental volume leads to the following general equation:

$$\frac{dU}{dt} = d\dot{Q}_{IN} + \dot{q}_x sdy + \dot{q}_y sdx - d\dot{W} - d\dot{Q}_{OUT} - \dot{q}_{x+dx} sdy - \dot{q}_{y+dy} sdx \quad (1)$$

where $d\dot{Q}_{IN}$ and $d\dot{Q}_{OUT}$ are the general expression of the heat flow rate

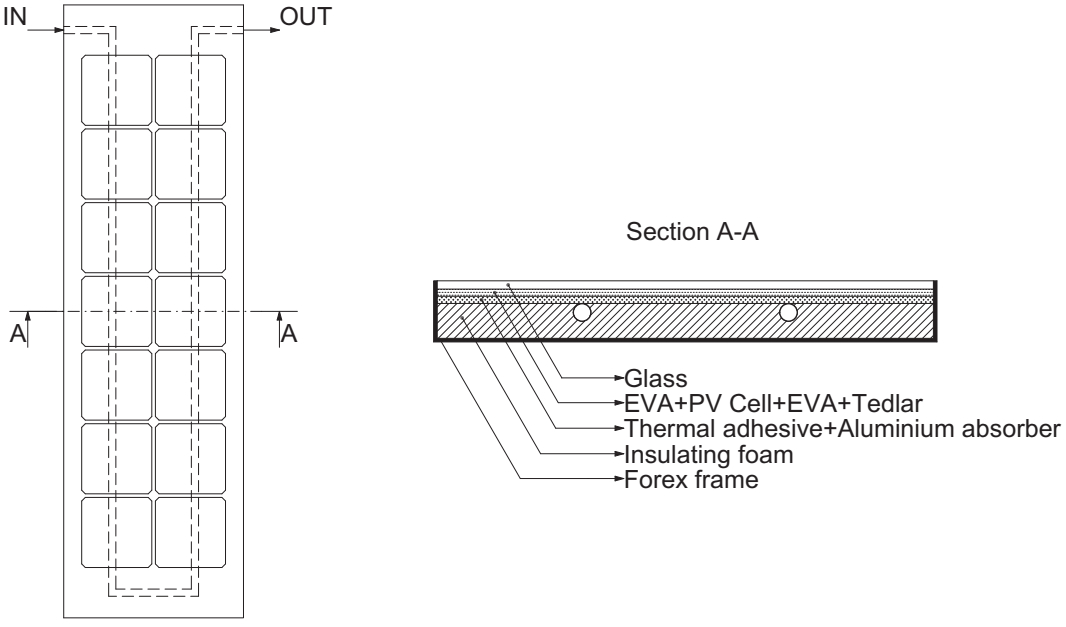

Fig. 1. Top-view and cross-section of the hybrid PV/T solar tile considered.

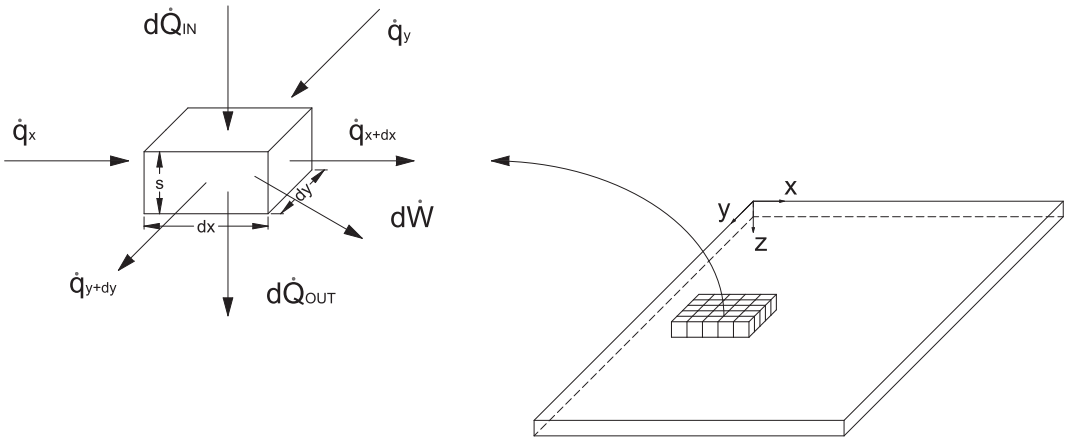

Fig. 2. Energy balance on the elemental volume of the hybrid PV/T solar tile.

that may be the conductive heat transfer between elemental volumes in neighbouring layers or the convective and radiative heat transfer with air, glass, PV or frame elemental volume. The mathematical expression of these terms is specific to the different layers and is detailed in the next sections. Similarly, $d\dot{W}$ represents the electric power produced in the elemental volume and is zero for each elemental volume apart for those in the PV layer. The mathematical model of the elemental volume power production is described in Section 2.2.

Assuming that the thermophysical properties of the material are constant due to the limited temperature operating range, introducing the Fourier's law and using Taylor's series for the last two terms in Eq. (1), the general form of the unsteady energy equation becomes:

$$\rho sc\frac{\partial T}{\partial t} = \frac{d\dot{Q}_{IN}}{dxdy} - \frac{d\dot{W}}{dxdy} - \frac{d\dot{Q}_{OUT}}{dxdy} - k\left(\frac{\partial^2 T}{\partial x^2} + \frac{\partial^2 T}{\partial y^2}\right) \tag{2}$$

As stated, the form of Eq. (2) changes as a function of the particular layer considered as detailed in the following sections.

2.1.1. Glass layer

For the glass layer, the net inlet heat flow rate is the absorbed solar irradiance, including the multiple reflection phenomenon between the glass layer and the PV layer, whereas the outlet heat flow rate accounts for the conductive heat transfer with the first EVA layer, the convective heat transfer with the air and the radiative heat transfer with the sky, the ground and the PV layer. Under the hypothesis that the glass optical properties are constant and assuming that the sky behaves like a blackbody, Eq. (2) becomes:

$$\begin{aligned}(\rho sc)_G\frac{\partial T_G}{\partial t} = {} & \alpha_{O,G}\left(1 + \frac{\tau_{O,G}\rho_{O,PV}}{1-\rho_{O,G}\rho_{O,PV}}\right)G - \frac{T_G - T_{EVA,1}}{\frac{1}{2}\left[\left(\frac{s}{k}\right)_G + \left(\frac{s}{k}\right)_{EVA,1}\right]} - h_{G-AIR}(T_G - T_{AIR}) + \\ & - \varepsilon_{O,G}\sigma F_{G-SKY}(T_G^4 - T_{SKY}^4) - \varepsilon_{O,G}\sigma F_{G-GND}(T_G^4 - T_{AIR}^4) - \frac{\sigma(T_G^4 - T_{PV}^4)}{\frac{1}{\varepsilon_{O,G}} + \frac{1}{\varepsilon_{O,PV}} - 1} \\ & - k_G\left(\frac{\partial^2 T_G}{\partial x^2} + \frac{\partial^2 T_G}{\partial y^2}\right)\end{aligned} \tag{3}$$

The air-to-glass convective heat transfer coefficient h_{G-AIR} that appears in Eq. (3) is estimated according to the correlation proposed by Watmuff [18] in forced convection regime, i.e. when $Gr/Re^2 \ll 1$ [19]:

$$Nu_{G-AIR,FC} = \frac{(2.8 + 3v_{AIR})L}{k_{AIR}} \tag{4}$$

vice versa, in natural convection regime, i.e. when $Gr/Re^2 \gg 1$ [19], the Churchill and Chu [20] correlation is adopted:

$$Nu_{G-AIR,NC} = 0.68 + 0.67Ra_L^{1/4}\left[1 + \left(\frac{0.492}{Pr}\right)^{9/16}\right]^{-4/9} \tag{5}$$

Finally, for mixed convection regime, i.e. when $Gr/Re^2 \approx 1$, the two previous correlations are combined together [19]:

$$Nu_{G-AIR,MC} = \sqrt[3]{Nu_{G-AIR,FC}^3 + Nu_{G-AIR,NC}^3} \tag{6}$$

Regarding the radiative heat transfer, in Eq. (3) it is assumed that the ground temperature is equal to the ambient temperature for simplicity, whereas the sky temperature is calculated using Swibank [21], Berdhal and Martin [22] or Aubinet [23] models according to the following equations:

$$T_{SKY} = \begin{cases} 0.0552T_{AIR}^{1.5} & \Leftrightarrow G \leqslant 100\ \mathrm{W\ m^{-2}} \\ T_{AIR}\left[0.711 + 0.0056T_{DP} + 0.000073T_{DP} + 0.013\cos(t)\right]^{\frac{1}{4}} & \Leftrightarrow G_{DIF}/G \leqslant 0.7 \\ 94 + 12.6\ln(p_{SAT}(T_{AIR})) - 13(G_H/1360) + 0.341T_{AIR} & \Leftrightarrow G_{DIF}/G > 0.7 \end{cases} \tag{7}$$

where the air dew point temperature T_{DP} has to be expressed in Celsius degree and the time t has to be expressed in hour from midnight. The ratio G_{DIF}/G is adopted to distinguish between a clear sky ($G_{DIF}/G \leqslant 0.7$) or a cloudy sky condition ($G_{DIF}/G > 0.7$).

Finally, the glass-to-sky and the glass-to-ground view factors are respectively calculated as follow:

$$F_{G-SKY} = \frac{1 + \cos(\theta)}{2} \tag{8}$$

$$F_{G-GND} = \frac{1 - \cos(\theta)}{2} \tag{9}$$

2.1.2. First EVA layer

Under the assumption that the EVA layer is a non-participating medium, the inlet and outlet heat flow rates at first EVA layer elemental volume are the conductive heat fluxes with the glass layer and with the PV layer respectively:

$$\begin{aligned}(\rho sc)_{EVA,1}\frac{\partial T_{EVA,1}}{\partial t} = {} & \frac{T_G - T_{EVA,1}}{\frac{1}{2}\left[\left(\frac{s}{k}\right)_G + \left(\frac{s}{k}\right)_{EVA,1}\right]} - \frac{T_{EVA,1} - T_{PV}}{\frac{1}{2}\left[\left(\frac{s}{k}\right)_{EVA,1} + \left(\frac{s}{k}\right)_{PV}\right]} \\ & - k_{EVA,1}\left(\frac{\partial^2 T_{EVA,1}}{\partial x^2} + \frac{\partial^2 T_{EVA,1}}{\partial y^2}\right)\end{aligned} \tag{10}$$

2.1.3. PV layer

For the PV layer, the inlet heat flow rates are the absorbed solar irradiance, incluiding, the multiple reflection phenomenon between the glass layer and the PV layer itself, the conductive heat flux with the first EVA layer and the radiative heat flux with the glass. The outlet heat flow rate is the conductive heat flux with the second EVA layer, but the term representing the elemental volume power production has to be accounted for in the elemental volume energy equation. Therefore, for

the PV layer Eq. (2) becomes:

$$(\rho sc)_{PV}\frac{\partial T_{PV}}{\partial t} = \left(\frac{\alpha_{O,PV}\tau_{O,G}}{1-\rho_{O,G}\rho_{O,PV}}\right)G + \frac{T_{EVA,1}-T_{PV}}{\frac{1}{2}\left[\left(\frac{s}{k}\right)_{EVA,1}+\left(\frac{s}{k}\right)_{PV}\right]} + \frac{\sigma\left(T_G^4-T_{PV}^4\right)}{\frac{1}{\varepsilon_{O,G}}+\frac{1}{\varepsilon_{O,PV}}-1} + - \frac{T_{PV}-T_{EVA,2}}{\frac{1}{2}\left[\left(\frac{s}{k}\right)_{PV}+\left(\frac{s}{k}\right)_{EVA,2}\right]} - k_{PV}\left(\frac{\partial^2 T_{PV}}{\partial x^2}+\frac{\partial^2 T_{PV}}{\partial y^2}\right) - \frac{d\dot{W}}{dxdy} \tag{11}$$

The last term that appears in Eq. (11), the elemental volume electric power production, is calculated as discussed in Section 2.2.

2.1.4. Second EVA layer, Tedlar layer and thermal adhesive layer

For the second EVA layer, the inlet and outlet heat flow rates at elemental volume level are the conductive heat fluxes with the photovoltaic layer and with the Tedlar layer respectively:

$$(\rho sc)_{EVA,2}\frac{\partial T_{EVA,2}}{\partial t} = \frac{T_{PV}-T_{EVA,2}}{\frac{1}{2}\left[\left(\frac{s}{k}\right)_{PV}+\left(\frac{s}{k}\right)_{EVA,2}\right]} + - \frac{T_{EVA,2}-T_{TD}}{\frac{1}{2}\left[\left(\frac{s}{k}\right)_{EVA,2}+\left(\frac{s}{k}\right)_{TD}\right]} - k_{EVA,2}\left(\frac{\partial^2 T_{EVA,2}}{\partial x^2}+\frac{\partial^2 T_{EVA,2}}{\partial y^2}\right) \tag{12}$$

Vice-versa, for the Tedlar layer, the conductive heat fluxes with the second EVA layer and with the thermal adhesive layer are the inlet and outlet heat flow rates at elemental volume respectively:

$$(\rho sc)_{TD}\frac{\partial T_{TD}}{\partial t} = \frac{T_{EVA,2}-T_{TD}}{\frac{1}{2}\left[\left(\frac{s}{k}\right)_{EVA,2}+\left(\frac{s}{k}\right)_{TD}\right]} - \frac{T_{TD}-T_{TA}}{\frac{1}{2}\left[\left(\frac{s}{k}\right)_{TD}+\left(\frac{s}{k}\right)_{TA}\right]} - k_{TD}\left(\frac{\partial^2 T_{TD}}{\partial x^2}+\frac{\partial^2 T_{TD}}{\partial y^2}\right) \tag{13}$$

Finally, for the thermal adhesive layer, the inlet and outlet heat flow rates at elemental volume level are the conductive heat fluxes with the Tedlar layer and the absorber plate layer respectively:

$$(\rho sc)_{TA}\frac{\partial T_{TA}}{\partial t} = \frac{T_{TD}-T_{TA}}{\frac{1}{2}\left[\left(\frac{s}{k}\right)_{TD}+\left(\frac{s}{k}\right)_{TA}\right]} - \frac{T_{TA}-T_A}{\frac{1}{2}\left[\left(\frac{s}{k}\right)_{TA}+\left(\frac{s}{k}\right)_{A}\right]} - k_{TA}\left(\frac{\partial^2 T_{TA}}{\partial x^2}+\frac{\partial^2 T_{TA}}{\partial y^2}\right) \tag{14}$$

2.1.5. Absorber plate layer

For the absorber plate layer, the inlet heat flow rate at elemental volume level has to consider the conductive heat transfer with the thermal adhesive layer whereas the outlet heat flow rate depends on the material found beneath it. If the elemental volume is above the insulating foam layer, the conductive heat transfer with it has to be accounted for and Eq. (2) becomes:

$$(\rho sc)_{A}\frac{\partial T_{A}}{\partial t} = \frac{T_{TA}-T_A}{\frac{1}{2}\left[\left(\frac{s}{k}\right)_{TA}+\left(\frac{s}{k}\right)_{A}\right]} - \frac{T_A-T_{IF,1}}{\frac{1}{2}\left[\left(\frac{s}{k}\right)_{A}+\left(\frac{s}{k}\right)_{IF,1}\right]} - k_A\left(\frac{\partial^2 T_A}{\partial x^2}+\frac{\partial^2 T_A}{\partial y^2}\right) \tag{15}$$

On the other side, when a tube is found beneath the absorber plate elemental volume, the outlet heat flow rate is the conductive heat flux with it and Eq. (2) becomes:

$$(\rho sc)_{A}\frac{\partial T_{A}}{\partial t} = \frac{T_{TA}-T_A}{\frac{1}{2}\left[\left(\frac{s}{k}\right)_{TA}+\left(\frac{s}{k}\right)_{A}\right]} - \frac{T_A-T_T}{\frac{1}{2}\left[\left(\frac{s}{k}\right)_{A}+\left(\frac{ln(D_{T,OUT}/D_{T,IN})}{2\pi kdl}\right)_{T}\right]+R_{TC}} - k_A\left(\frac{\partial^2 T_A}{\partial x^2}+\frac{\partial^2 T_A}{\partial y^2}\right) \tag{16}$$

where dl represents the length of the tube in the flow direction and is equal to dx when the absorber plate elemental volume is above a portion of tube where the water flows in x direction, to dy when the elemental volume is above a portion of tube where the water flows in y direction or their average when the elemental volume is on the tube bend.

2.1.6. Tube and heat transfer fluid

For the tube, the inlet heat flow rate at elemental volume level is the conductive heat flux with the absorber plate, whereas the outlet heat flow rate accounts for the conductive heat transfer with the insulating foam layer and the convective heat transfer with the coolant flow rate:

$$(\rho c)_T\frac{D_{T,OUT}^2-D_{T,IN}^2}{2D_{T,OUT}}\frac{\partial T_T}{\partial t} = \frac{T_A-T_T}{\frac{1}{2}\left[\left(\frac{s}{k}\right)_{A}+\left(\frac{ln(D_{T,OUT}/D_{T,IN})}{2\pi kdl}\right)_{T}\right]+R_{TC}} - \frac{T_{IF,1}-T_T}{\frac{1}{2}\left[\left(\frac{s}{k}\right)_{IF,1}+\left(\frac{ln(D_{T,OUT}/D_{T,IN})}{2\pi kdl}\right)_{T}\right]} + - \frac{T_T-T_{IF,2}}{\frac{1}{2}\left[\left(\frac{ln(D_{T,OUT}/D_{T,IN})}{2\pi kdl}\right)_{T}+\left(\frac{s}{k}\right)_{IF,2}\right]} - \frac{d\dot{Q}_{T-HTF}}{dyD_{T,OUT}/2} \tag{17}$$

In Eq. (17), IF,1 and IF,2 are the two sub-layers the insulating foam is supposed to be composed of as detailed in the next section. Moreover, the last term that appears in the same equation is the convective heat flow rate between the tube and the heat transfer fluid and is modelled as detailed below.

Regarding the heat transfer fluid, at elemental volume level, the inlet heat flow rate consists of the inlet fluid advective heat flux and the convective heat flux between the tube and the coolant fluid itself, whereas the outlet heat flow rate is made up by the outlet fluid advective heat flux:

$$(Mc_P)_{HTF}\frac{\partial T_{HTF}}{\partial t} = -(\dot{m}c_P)_{HTF}\frac{\partial T_{HTF}}{\partial l}dl + d\dot{Q}_{T-HTF} \tag{18}$$

In the proposed approach, a new way of modelling the convective heat transfer between the tube and the heat transfer fluid is introduced. Indeed, as shown in Fig. 3, the heat flux from the tube to the heat

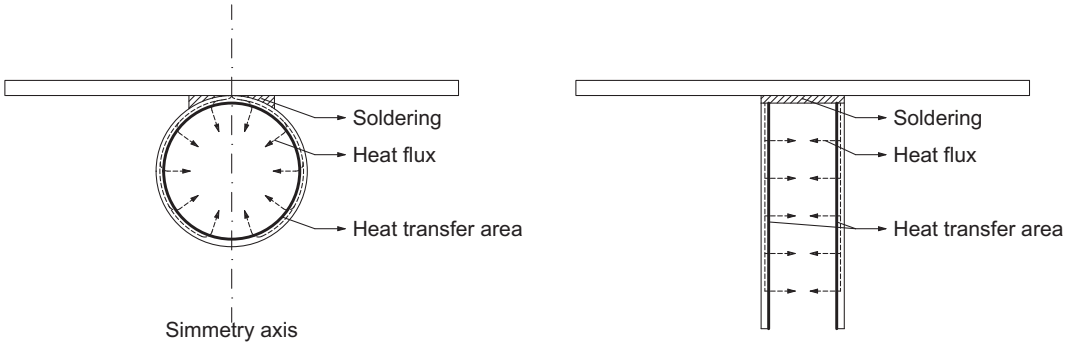

Fig. 3. Actual tube representation (left) and equivalent fins representation (right).

transfer fluid is modelled dividing the cross-section of the tube in two symmetrical parts and assuming that each half-tube behaves like a straight fin with adiabatic tip of length equal to half circumference. Consequently, the convective heat transfer between the tube and the coolant fluid of each fin may be calculated as follow:

$$\frac{d\dot{Q}_{T-HTF}}{2} = \pi\frac{D_{T,IN}}{2}\eta h_{HTF}(T_T - T_{HTF})dl \tag{19}$$

Where the convective heat transfer coefficient is calculated according to the most recent version of the Gnielinski's correlation [24], whereas the fin efficiency is calculated according to the following equation:

$$\eta = \frac{\tanh(\sqrt{2h_{T-HTF}/(k_T s_T)}\,dl)}{\sqrt{2h_{T-HTF}/(k_T s_T)}\,dl} \tag{20}$$

Assuming the coolant as an incompressible fluid and neglecting, for the sake of simplicity, the tube thermal resistance in the energy equation only, the final form of the heat transfer fluid energy equation as follows:

$$(\rho c_P)_{HTF}\frac{\partial T_{HTF}}{\partial t} = -(\rho c_P)_{HTF} v_{HTF}\frac{\partial T_{HTF}}{\partial l} + \frac{4\eta h_{HTF}}{D_{T,IN}}(T_T - T_{HTF}) \tag{21}$$

2.1.7. Insulating foam layer

As stated, in the proposed model the temperature is supposed to be uniform in the z direction. Although this assumption is accurate for thin or high thermal conductivity layers, it could lead to poor result for thick or low thermal conductivity layers such as the insulating foam one. Consequently, in order to improve the model accuracy, the insulating foam layer is divided in two sub-layers with different thickness: the first insulating foam sub-layer thickness is equal to tube outer diameter whereas the thickness of the second sub-layer is complementary to the overall insulating foam thickness.

For the first insulating foam sub-layer, the outlet heat flow rate term in Eq. (2) depends on the elemental volume position in the sub-layer. Indeed, if all the neighbouring elemental volumes in the x–y plane are in the insulating foam sub-layer, this term is a pure conduction term and Eq. (2) becomes:

$$(\rho sc)_{IF,1}\frac{\partial T_{IF,1}}{\partial t} = \frac{T_A - T_{IF,1}}{\frac{1}{2}\left[\left(\frac{s}{k}\right)_A + \left(\frac{s}{k}\right)_{IF,1}\right]} - \frac{T_{IF,1} - T_{IF,2}}{\frac{1}{2}\left[\left(\frac{s}{k}\right)_{IF,1} + \left(\frac{s}{k}\right)_{IF,2}\right]} - k_{IF}\left(\frac{\partial^2 T_{IF,1}}{\partial x^2} + \frac{\partial^2 T_{IF,1}}{\partial y^2}\right) \tag{22}$$

Vice-versa, if one of the neighbouring elemental volume in the x–y plane is in the tube, Eq. (2) changes as follows:

$$(\rho sc)_{IF,1}\frac{\partial T_{IF,1}}{\partial t} = \frac{T_A - T_{IF,1}}{\frac{1}{2}\left[\left(\frac{s}{k}\right)_A + \left(\frac{s}{k}\right)_{IF,1}\right]} - \frac{T_{IF,1} - T_T}{\frac{1}{2}\left[\left(\frac{s}{k}\right)_{IF,1} + \left(\frac{\ln(D_{T,OUT}/D_{T,IN})}{2\pi k dl}\right)_T\right]} - k_{IF,1}\left(\frac{\partial^2 T_{IF,1}}{\partial x^2} + \frac{\partial^2 T_{IF,1}}{\partial y^2}\right) \tag{23}$$

For the second insulating foam sub-layer, the outlet heat flow rate at elemental volume level is the conductive heat flux with the Forex layer whereas the inlet heat flow rate depends on the material found above it. If the elemental volume is below the insulating foam first sub-layer, the inlet heat flow rate is the conductive heat flux with it and Eq. (2) becomes:

$$(\rho sc)_{IF,2}\frac{\partial T_{IF,2}}{\partial t} = \frac{T_{IF,1} - T_{IF,2}}{\frac{1}{2}\left[\left(\frac{s}{k}\right)_{IF,1} + \left(\frac{s}{k}\right)_{IF,2}\right]} - \frac{T_{IF,2} - T_F}{\frac{1}{2}\left[\left(\frac{s}{k}\right)_{IF,2} + \left(\frac{s}{k}\right)_F\right]} - k_{IF}\left(\frac{\partial^2 T_{IF,2}}{\partial x^2} + \frac{\partial^2 T_{IF,2}}{\partial y^2}\right) \tag{24}$$

On the other side, when a tube is found above the elemental volume in the second insulating foam sub-layer, the inlet heat flow rate becomes the conductive heat flux with the tube and Eq. (2) becomes:

$$(\rho sc)_{IF,2}\frac{\partial T_{IF,2}}{\partial t} = \frac{T_T - T_{IF,2}}{\frac{1}{2}\left[\left(\frac{\ln(D_{T,OUT}/D_{T,IN})}{2\pi k dl}\right)_T + \left(\frac{s}{k}\right)_{IF,2}\right]} - \frac{T_{IF,2} - T_F}{\frac{1}{2}\left[\left(\frac{s}{k}\right)_{IF,2} + \left(\frac{s}{k}\right)_F\right]} - k_{IF}\left(\frac{\partial^2 T_{IF,2}}{\partial x^2} + \frac{\partial^2 T_{IF,2}}{\partial y^2}\right) \tag{25}$$

2.1.8. Forex layer

Finally, for the Forex layer (back cover), the inlet heat flow rate is the conductive heat flux with the second insulating foam layer, whereas the outlet heat flow rate accounts for the convective heat transfer with the air and the radiative heat transfer with the sky and the ground. Therefore Eq. (2) becomes:

$$(\rho sc)_F\frac{\partial T_F}{\partial t} = \frac{T_{IF,2} - T_F}{\frac{1}{2}\left[\left(\frac{s}{k}\right)_{IF,2} + \left(\frac{s}{k}\right)_F\right]} - h_{F-AIR}(T_F - T_{AIR}) - \varepsilon_{O,F}\sigma F_{F-SKY}(T_F^4 - T_{SKY}^4) + - \varepsilon_{O,F}\sigma F_{F-GND}(T_F^4 - T_{AIR}^4) - k_F\left(\frac{\partial^2 T_F}{\partial x^2} + \frac{\partial^2 T_F}{\partial y^2}\right) \tag{26}$$

where the air-to-Forex convective heat transfer coefficient h_{F_AIR} is calculated using the same set of equations used to calculate the air-to-glass convective heat transfer coefficient, Eqs. (4)–(6), whereas the Forex-to-sky and the Forex-to-ground view factors are respectively calculated as follow:

$$F_{F-SKY} = \frac{1-\cos(\theta)}{2} \tag{27}$$

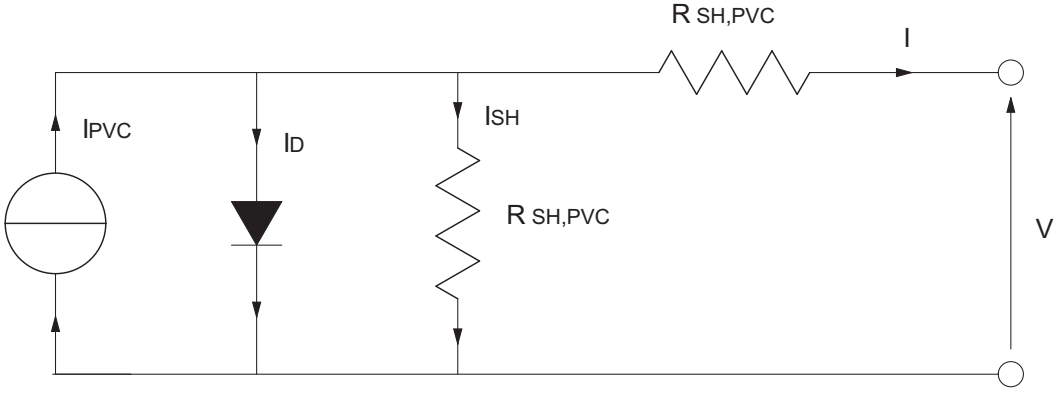

Fig. 4. Five parameters model equivalent circuit.

$$F_{F-GND} = \frac{1 + \cos(\theta)}{2} \tag{28}$$

The system of non-linear equation resulting from the forth-order energy equation written for each elemental volume is solved in MATLAB environment using Newton-Raphson's algorithm with an upwind numerical scheme for the water energy equation.

2.2. PV layer electrical model

The electrical model of the PV layer is developed according to Migliorini et al. [25], where the five parameters equivalent electrical circuit for the PV cell representation is considered. The five parameters equivalent circuit is shown in Fig. 4 and consists of a current generator, a diode representing the electrical behaviour of the PN junction and two resistances, the cell shunt resistance and the cell series resistance, that represent the cell recombination loss and the cell Ohmic loss respectively. According to this model, the current produced by a single PV cell is calculated by the following equation:

$$I = I_{PVC} - I_D - I_{SH} = I_{PV} - I_0 \left[\exp\left(\frac{V + R_{S,PVC} I}{n V_{TH}} - 1 \right) \right] - \left(\frac{V + R_{S,PVC} I}{R_{SH,PVC}} \right) \tag{29}$$

with

$$V_{TH} = \frac{k_B T_{PVC}}{e^-} \tag{30}$$

The five parameters that appear in Eq. (29) can be determined either using the I-V characteristic reported in the manufacturer's datasheet or starting from measured values, being the latter the approach adopted in the present paper as suggested in [26] and detailed in Section 3. Finally, the dependence of the parameters on the solar radiation and on the PN junction temperature is accounted for according to De Soto et al. [27]:

$$I_{PVC} = \frac{G}{G_{REF}} \{ I_{PVC,REF} [1 + \alpha_{I_{SC}} (T_{PVC} - T_{PVC,REF})] \} \tag{31}$$

$$I_0 = I_{0,REF} \left(\frac{T_{PVC}}{T_{PVC,REF}} \right)^3 \exp\left[\frac{1}{n k_B} \left(\frac{E_{G,REF}}{T_{PVC,REF}} - \frac{E_G}{T_{PVC}} \right) \right] \tag{32}$$

$$n = n_{REF} \tag{33}$$

$$R_{S,PVC} = R_{S,PVC,REF} \tag{34}$$

$$R_{SH,PVC} = R_{SH,PVC,REF} \frac{G_{REF}}{G} \tag{35}$$

The set of previous equations is solved in order to find the $I-V$ curve of a single PV cell. However, particular attention has to be put in solving these equations because of their dependency on PV cell temperature, but usually from the thermal point of view more than one elemental volume is found for each of them. Consequently, in the present model, the strategy of identifying all the elemental volumes inside each PV cell and finding their maximum temperature is adopted: this is a conservative approach since the highest temperature corresponds to the lowest cell voltage, i.e. to the lowest cell conversion efficiency. Once this value is determined, Eqs. (29)–(35) are first solved to compute the $I-V$ characteristic of each PV cell and, then, all the $I-V$ curves of PV cells are summed together at the same current since the PV cells are connected in series. Ultimately, the PV module $I-V$ curve is obtained and a Maximum Power Point Tracking (MPPT) algorithm is applied in order to find the optimal $I-V$ pair which guarantees the PV layer maximum power production (from a practical point of view, the maximum power condition is guaranteed by the maximum power point tracker connected to the PV module). Once the optimal current is known, it is back applied to the $I-V$ characteristic of each PV cell to compute the single PV cell, and, thus, elemental volume power to be put in Eq. (2).

3. Experimental set-up

In order to validate the model described in Section 2, an experimental campaign on two hybrid PV/T solar tiles was carried out at the laboratory SolarTech^{Lab}, Politecnico di Milano, whose latitude and longitude are 45°30′10.588″N and 9°9′23.677″E respectively [28]. Each hybrid PV/T collector is 1826 mm long and 259 mm width, consists of 28 mono-crystalline silicon cells (100 mm × 100 mm each, glass area equal to 0.32 m^2) with a nominal power production equal to 75 W and uses the sheet-and-tube technology for heat removal. The main optical and thermophysical features of each hybrid PV/T tile are summarised in Table 1 whereas the measured electrical characteristics of each PV cell are reported in Table 2. With the aim of increasing the measurement accuracy, the two hybrid PV/T solar tiles were first connected in series, both electrically and hydraulically, and then installed in the hydronic loop shown in Fig. 5. The hybrid PV/T tiles azimut and tilt angles were set to −6°30′ (assuming 0° as south direction and counting clockwise) and to 27° respectively. It is worth specifying that the electrical connection in series was mandatory to obtain the optimization of the PV layer power production since the micro-inverter used in the experimental set-up was designed for typical PV panels, which usually consists of 60 cells, and, consequently, its MPPT voltage range was about twice the one of a single hybrid PV/T tile. Moreover, in the hydronic loop a broad range of testing conditions was allowed by the use of an inverter driven pump, a 3-way valve and a dry cooler equipped with two variable speed fans.

The hybrid PV/T solar tiles performance was assessed through a direct measure of the power production, by means of the use of the just discussed micro-inverter, and through an indirect measure of the heat flow rate, by means of the use of a vortex flow rate measurement device for the water flow rate and two 4-wires Pt100 RTD for the water inlet and outlet temperatures. Finally, the environmental conditions were measured with a meteorological station equipped with three pyranometers, for the measurement of the total and diffuse irradiance on horizontal plane and on a 30° plane respectively, with a Pt100 RTD, for the measurement of air temperature, and with a cup anemometer, for the measurement of wind velocity. Other measurement instruments

Table 1
Optical and thermophysical properties of each layer of the PV/T tile.

Material	s [mm]	α_O [–]	ε_O [–]	τ_O [–]	ρ_O [–]	ρ [kg m^{-3}]	c [J kg^{-1} K^{-1}]	k [W m^{-1} K^{-1}]
Glass	3.6	0.015	0.9	0.9	0.078	2480	750	1.10
EVA	0.4	–	–	–	–	1430	1130	0.35
PV	0.3	0.90	0.96	0	0.1	2330	705.5	148
EVA	0.4	–	–	–	–	1430	1130	0.35
Tedlar	0.2	–	–	–	–	1450	1300	0.13
Glue	0.1	–	–	–	–	1060	980	1.40
Plate	4.0	–	–	–	–	2700	896	167
Insulation	19.3	–	–	–	–	150	1000	0.0148
Forex	1.0	0	0.82	0	0.18	150	1000	0.0190

Table 2
Electrical parameters of each PV cell.

Parameter	Value
$I_{PVC,REF}$ [A]	5.7900
$I_{0,REF}$ [A]	$2.9282 \cdot 10^{-10}$
n_{REF} [–]	1.0599
$R_{S,PVC,REF}$ [Ω]	$7.7083 \cdot 10^{-3}$
$R_{SH,PVC,REF}$ [Ω]	$250 \cdot 10^{3}$

were provided with the meteorological station but were not used in the present study (e.g. air humidity, wind direction and rain precipitation sensors). More details about instrumentations are found in [28,26]. The main characteristics of all the measurement devices are collected in Table 3.

Working data of the hybrid PV/T solar tiles were sampled every second whereas weather data were sampled every ten second. Since the wind speed data were recorded at the anemometer height (3 m) instead of hybrid PV/T solar tiles height (0.7 m), the correction procedure suggested by Kaplani and Kaplanis [29] was used:

$$\frac{v_{AIR}}{v_{AIR,REF}} = \left(\frac{z}{z_{REF}}\right)^{n} \tag{36}$$

where n is the exponent that represents the boundary layer profile and is calculated as follows:

$$n = \frac{0.37 - 0.0881 \ln(v_{AIR,REF})}{1 - 0.0881 \ln(z_{REF}/10)} \tag{37}$$

4. Results and discussion

A two weeks experimental campaign was carried out using the experimental facility described in the previous section. Hereinafter, the experimental results are not described in detail since the objective of the paper is to present and validate the model. All the tests were carried out adopting the same procedure and using a constant water flow rate equal to 96 kg h^{-1}. More in detail, during clear sky days, the water temperature at collectors inlet was let to vary depending on the weather conditions for the first part of the test, whereas during the second part of the test sudden temperature variations were set acting cyclically on the 3-way valve and on the dry cooler fan speed shown in Fig. 5. In this way, during the same test it was possible to measure operating data under both smooth variation and steep working conditions variations. Therefore, the same test could be used to validate the model with both slowly changing and rapidly changing boundary conditions. Vice-versa, during cloudy days, the water temperature at collectors inlet was let to vary as a function of weather conditions only without any action on the 3-way valve and on the dry cooler fan. Finally, even if the experimental campaign lasted nine days, the results in terms of power production and water outlet temperature are shown only for three selected days for the brevity. It is worth specifying that the results shown in the following figures refer to the two hybrid PV/T solar tiles that are connected in series, i.e. the electrical power is that produced by the two tiles whereas the water outlet temperature is that at the outlet of the second tile.

First tests were carried out to evaluate the sole thermal part of the model described in Section 2. During these tests, the micro-inverter equipping the hybrid PV/T solar tiles was disconnected so that the two collectors behaved like a traditional unglazed solar collector ("thermal only" configuration). Fig. 6(a) shows the solar irradiance and the water inlet temperature during testing period, whereas the water outlet temperature, together with the difference between experimental and numerical value, are shown in Fig. 6(b). From the analysis of these figures it is possible to state that, in "thermal only" configuration, the developed model may accurately predict the water outlet temperature since the error between experimental and numerical data lies within −0.23 K to +0.51 K both under smooth (from 9:00 to 13:55) and steep (from 13:55 to 14:05 and at 15:55) variation of working conditions. This allows to conclude that, from the thermal point of view, the developed model is satisfying and no further calibrations are necessary. It is worth specifying that, from the simulation point of view, the "thermal only" configuration is simulated removing the $d\dot{W}$ term that appears in Eqs. (1) and (2), which means not solving all the equations reported in Section 2.2.

During the second group of tests, both the power and the heating capacity production as a function of weather conditions were measured to check the validity of the overall model. The values of solar irradiance and water inlet temperature during a clear sky day are reported in Fig. 7(a), whereas the comparison between the experimental and numerical trend of the power production and of the water outlet temperature are shown in Fig. 7(b) and (c) respectively. In the same figures, the differences between experimental and numerical value are reported to outline that, again, the model shows very good prediction capability

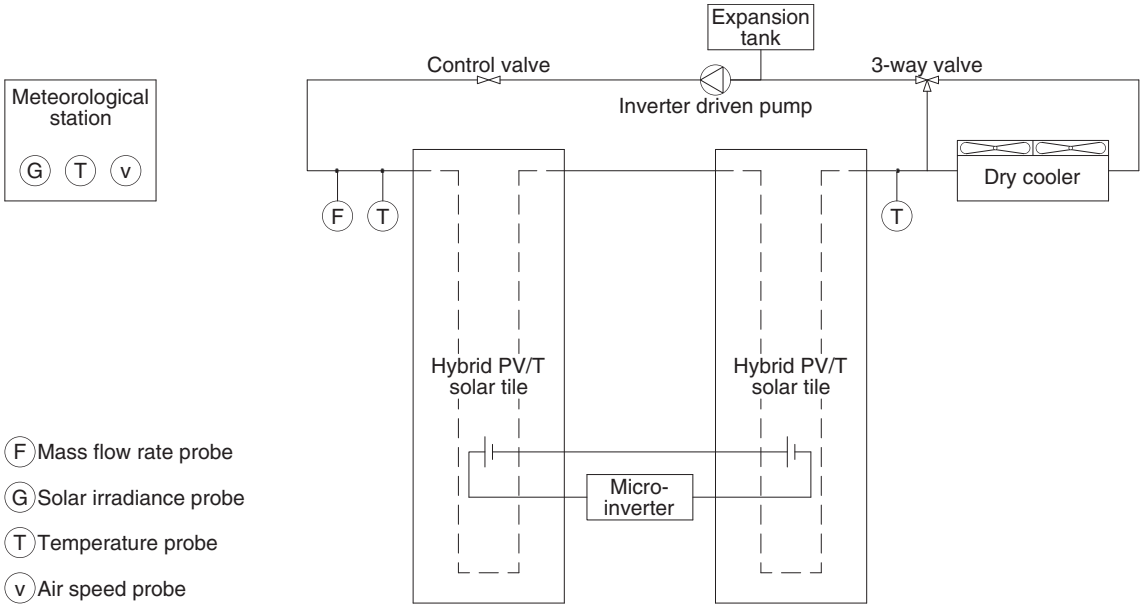

Fig. 5. Schematic representation of the experimental set-up.

Table 3
Metrological characteristics of the instrumentation.

Variable	Device type	Range	Uncertainty
Irradiance	Pyranometer	285–3000 nm	± 2% (daily basis)
Air speed	Cup anemometer	0–60 m s^{-1}	± 1.5%; v_{AIR} < 3 m s^{-1} ± 1%; v_{AIR} > 3 m s^{-1}
Air temperature	Pt100 1/3 DIN	243.15–343.15 K	± 0.2 K
Electrical power	Microinverter	0–750 W	± 1% f.s.
Water flow rate	Vortex	0.015–0.25 dm^3 s^{-1}	± 1% f.s.
Water temperature	Pt100 1/3 DIN	243.15–343.15 K	± 0.2 K

since the error lies within −3.9 W to 1.9 W and within −0.41 K to 0.25 K both under smooth (from 9:00 to 14:55) and steep (at 14:55, from 15:15 to 15:55 and from 16:40 to 17:00) variation of working conditions. A comparison between the results obtained without power production (Fig. 6) and with power production (Fig. 7) reveals that the model accuracy in predicting the water outlet temperature remains the same since the errors between experimental and numerical value are very similar. The reason is that, without power production, the not converted solar irradiance simply becomes an additional heat flux for the layers below the PV one, influencing the conduction and the convection phenomena already accounted for in the model. Consequently, it is possible to state that the model is able to correctly solve the thermal field inside the collector in any working conditions.

Similar results are found for a cloudy day as shown in Fig. 8. During cloudy day, the experimental set-up was operated without any sudden variation in the water-side temperature due to the high variability of the solar irradiance. In this situation, the model performance slightly decreases since the prediction of the power production lies now within −14.7 W to 15.4 W, whereas the prediction of the water outlet temperature spans the range −0.38 K to 0.53 K. This allows to conclude that the model is more sensitive to the sudden variation of solar irradiance than of the water inlet temperature because the former is the source of the collector operation.

Finally, additional tests without any sudden change in operating conditions, but with fixed water flow rate and fan speed, were carried out with the aim of measuring the energies and assessing the model capability in long-term prediction. The tests were run during clear sky and cloudy days with both “thermal only” and “electric + thermal” configurations. The experimental and numerical results, with their relative difference, are collected in Table 4 together with the solar irradiation on the horizontal plane. Looking at the electrical energy, the results show that the model is very accurate since the error in the prediction of the daily electrical energy production with respect to the experimental data is between −2.64% and +1.73%, where the larger difference is found during a cloudy sky day (Day 3). Vice-versa, from the thermal energy point of view, the model is slightly less accurate

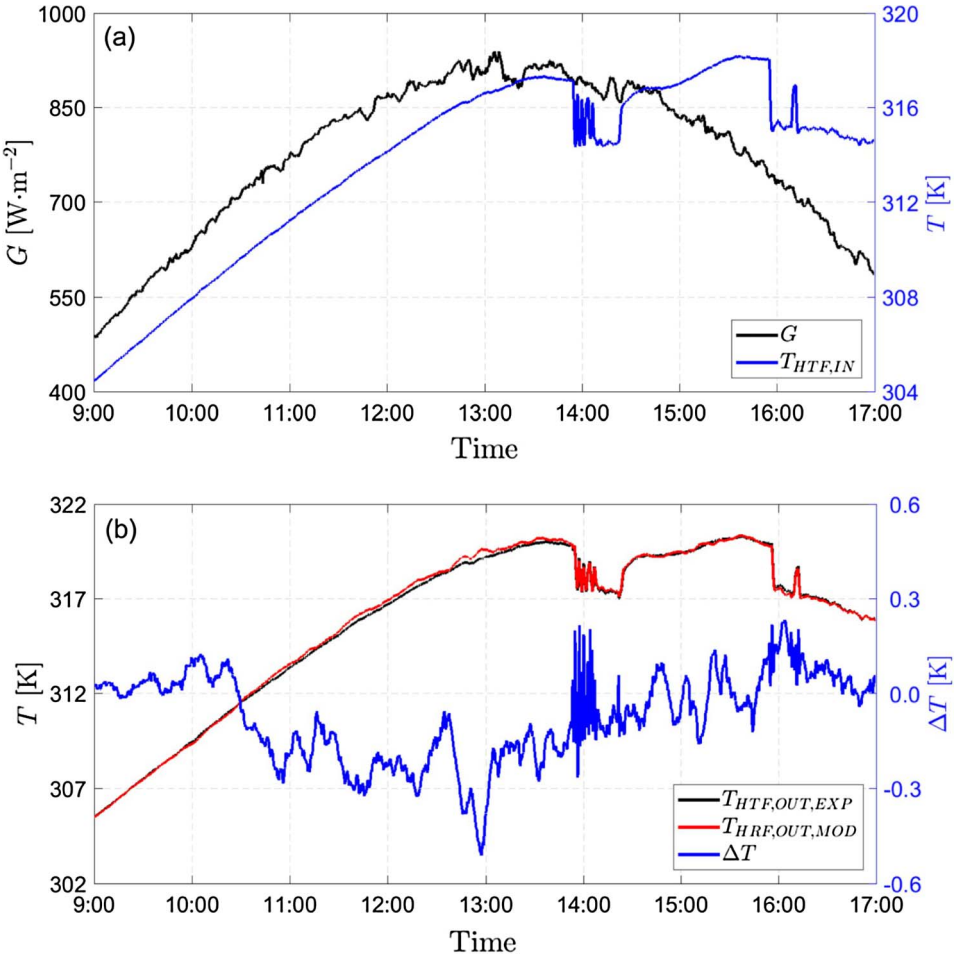

Fig. 6. Global radiation on horizontal plane and water inlet temperature (a) and experimental and numerical water outlet temperature together with their difference (b) for field test in “thermal only” working conditions during a clear sky day.

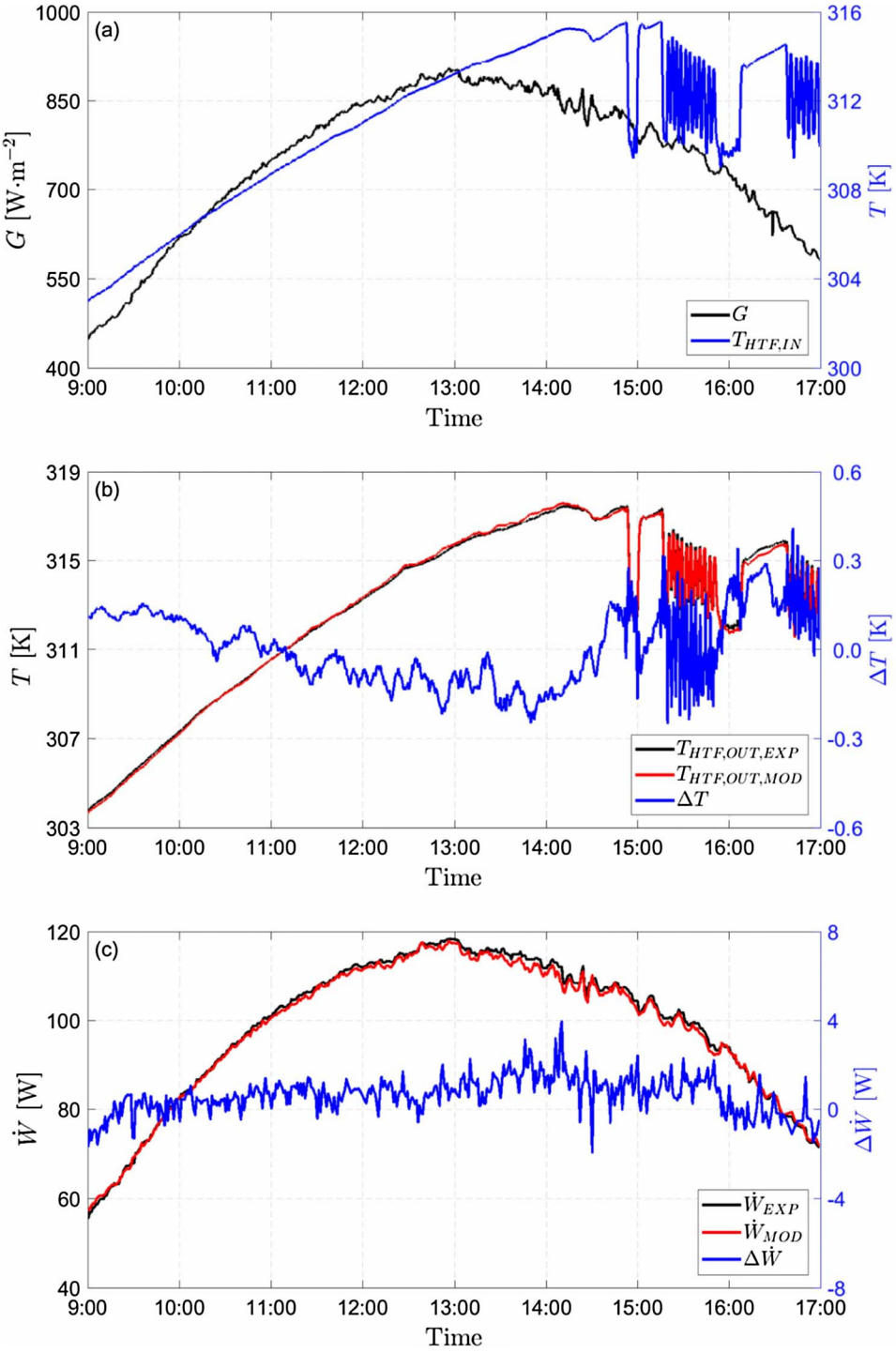

Fig. 7. Global radiation on horizontal plane and water inlet temperature (a), experimental and numerical water outlet temperature together with their difference (b) and experimental and numerical power production together with their difference (c) in "electric + thermal" working conditions for field test during a clear sky day.

with an error with respect to the experimental results in the range ± 5%, both in "thermal only" working conditions and in "electric + thermal" working conditions, with larger values during cloudy sky days. An exception is Day 1, where the error is equal to +7.37%, but that day was very cloudy as can be noted comparing the value of solar irradiation on horizontal plane with other days. During cloudy days, sudden and steep variations in solar irradiation and/or wind speed occurred, whereas during sunny days the transition was smoother. As a result, the input condition, i.e. weather data, to be used for simulations during cloudy days were strongly variable and this led to less accurate predictions. Consequently, it can be outlined that the model is strongly sensitive to steep solar irradiance variation, which is one of its limit.

Finally, the proposed model is compared to the models available in the scientific literature and discussed in Section 1. The comparison is carried out considering clear sky days only since it is the most frequent weather condition found in the previous available studies. During these days, the average root mean square percentage deviation of water temperature difference and power production was 0.178% and 1.05% respectively. Firstly, considering the instantaneous values of the power production and water outlet temperature, the proposed model performs better than those found in the open literature both from the power production point of view [9,10] and from the water outlet temperature point of view [4,8–10,15]. Secondly, considering the daily

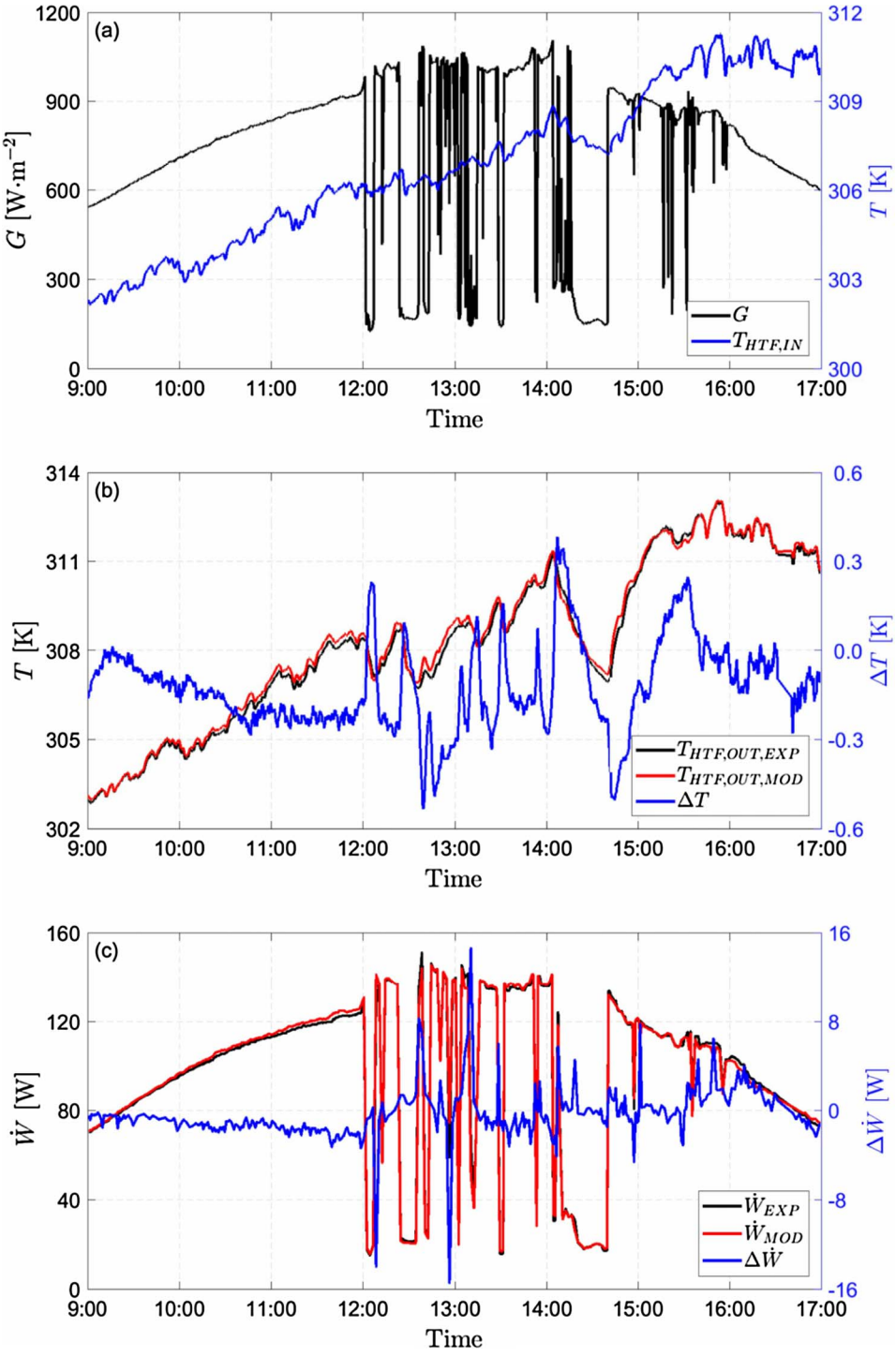

Fig. 8. Global radiation on horizontal plane and water inlet temperature (a), experimental and numerical water outlet temperature together with their difference (b) and experimental and numerical power production together with their difference (c) in "electric + thermal" working conditions for field test during a cloudy day.

Table 4
Comparison between experimental and numerical electrical and thermal energies for several days.

Day	E_{SUN} [MJ m^{-2}]	$E_{EL,EXP}$ [MJ]	$E_{EL,NUM}$ [MJ]	e_{EL} [%]	$E_{TH,EXP}$ [MJ]	$E_{TH,NUM}$ [MJ]	e_{TH} [%]
1	13.95	0.00	0.00	–	3.96	4.25	7.37%
2	28.92	0.00	0.00	–	8.12	8.22	1.28%
3	21.14	2.81	2.74	−2.64%	4.73	4.94	4.43%
4	24.13	3.12	3.18	1.73%	6.23	5.92	−4.90%
5	24.63	3.12	3.10	−0.63%	6.59	6.48	−1.67%
6	27.09	3.12	3.07	−1.62%	8.03	8.12	1.13%

performance, the proposed model is slightly more accurate for the electric energy prediction [11,12] or more accurate [2,10,13,16] with respect to those achieved with the models available in the open literature. From the thermal energy point of view, the model shows higher accuracy with respect to models proposed in [8,15,17]. As a conclusion, it is possible to state that the proposed model has better prediction capability than the those already available in the scientific literature.

5. Conclusions

In this paper, a comprehensive, 2D + 1D dynamic model of an unglazed, sheet-and-tube, hybrid PV/T solar collector is developed and

validated. The model uses the control-volume approach to solve the unsteady energy equation and the five parameter electric equivalent circuit to model the electrical behaviour. A dedicated experimental campaign on two hybrid PV/T solar tiles connected in series was carried out at SolarTech^{Lab} to validate the model. The results show that during clear sky days the developed model is able to predict the instantaneous power production within ± 4 W and the water outlet temperature within ± 0.5 K, whereas during variable sky days the prediction of the power production is slightly less accurate since an error in the range ± 15 W is found with an error for the water outlet temperature similar to clear sky conditions. On a daily basis, the calculated electrical and thermal energies agree within −2.64% to +1.73% and within −4.90% to +7.37% with experimental data respectively, with larger errors during cloudy days. Compared to previously published model, the one proposed in this paper shows generally better performance, resulting in a more accurate tool for unglazed, sheet-and-tube, hybrid PV/T collector simulation.

References

[1] H. Zondag, D. Vries, A.A. Van Steenhoven, W.G.J. Van Helden, R.J.C. Van Zolingen, The thermal and electrical yield of a combi-panel, in: Proceedings of ISES World Congress, Jerusalem, vol. 3, 1999, pp. 96–101.

[2] H.A. Zondag, D.W. De Vries, W.G.J. Van Helden, R.J.C. Van Zolingen, A.A. Van Steenhoven, The thermal and electrical yield of a PV-Thermal collector, Sol. Energy 72 (2002) 113–128, http://dx.doi.org/10.1016/S0038-092X(01)00094-9.

[3] T.T. Chow, Performance analysis of photovoltaic-thermal collector by explicit dynamic model, Sol. Energy 75 (2003) 143–152, http://dx.doi.org/10.1016/j.solener.2003.07.001.

[4] S. Bhattarai, J.-H. Oh, S.-H. Euh, G.K. Kafle, D.H. Kim, Simulation and model validation of sheet and tube type photovoltaic thermal solar system and conventional solar collecting system in transient states, Sol. Energy Mater. Sol. Cells 103 (2012) 184–193, http://dx.doi.org/10.1016/j.solmat.2012.04.017.

[5] N. Amrizal, D. Chemisana, J.I. Rosell, Hybrid photovoltaic-thermal solar collectors dynamic modeling, Appl. Energy 101 (2013) 797–807, http://dx.doi.org/10.1016/j.apenergy.2012.08.020.

[6] EN 12975, Thermal Solar Systems and Components - Solar Collectors, 2006.

[7] K. Touafek, A. Khelifa, M. Adouane, Theoretical and experimental study of sheet and tubes hybrid PVT collector, Energy Convers. Manage. 80 (2014) 71–77, http://dx.doi.org/10.1016/j.enconman.2014.01.021.

[8] A. Khelifa, K. Touafek, H.B. Moussa, Approach for the modelling of hybrid photovoltaic-thermal solar collector, IET Renew. Power Gener. 9 (2014) 207–217, http://dx.doi.org/10.1049/iet-rpg.2014.0076.

[9] P. Haurant, C. Ménézo, L. Gaillard, P. Dupeyrat, Dynamic numerical model of a high efficiency PV-T collector integated into a domestic hot water system, Sol. Energy 111 (2015) 68–81, http://dx.doi.org/10.1016/j.solener.2014.10.031.

[10] N. Aste, F. Leonforte, C. Del Pero, Design, modeling and performance monitoring of a photovoltaic-thermal PVT water collector, Sol. Energy 112 (2015) 85–99, http://dx.doi.org/10.1016/2014.11.025.

[11] N. Aste, C. Del Pero, F. Leonforte, M. Manfren, Performance monitoring and modeling of an uncovered photovoltaic-thermal PVT water collector, Sol. Energy 135 (2016) 551–568, http://dx.doi.org/10.1016/2016.06.029.

[12] O. Rejeb, H. Dhaou, A. Jemni, A numerical investigation of a photovoltaic thermal (PV/T) collector, Renew. Energy 77 (2015) 43–50, http://dx.doi.org/10.1016/j.renene.2014.12.012.

[13] C. Guo, J. Ji, W. Sun, J. Ma, W. He, Y. Wang, Numerical simulation and experimental validation of tri-functional photovoltaic/thermal solar collector, Energy 87 (2015) 470–480, http://dx.doi.org/10.1016/j.energy.2015.05.017.

[14] J. Ji, C. Guo, W. Sun, W. He, Y. Wang, G. Li, Experimental investigation of tri-functional photovoltaic/thermal solar collector, Energ. Convers. Manage. 88 (2014) 650–656, http://dx.doi.org/10.1016/j.enconman.2014.09.030.

[15] I. Guarracino, A. Mellor, N.J. Ekins-Daukes, C. Markides, Dynamic coupled thermal-and-electrical modelling of sheet-and-tube hybrid photovoltaic-thermal (PVT) collectors, Appl. Therm. Eng. 101 (2016) 778–795, http://dx.doi.org/10.1016/j.applthermaleng.2016.02.056.

[16] M. Hazami, A. Riahi, F. Mehdaoui, O. Nouicer, A. Farhat, Energetic and exergetic performances analysis of a PV/T (photovoltaic thermal) solar system tested and simulated under to Tunisian (North Africa) climatic conditions, Energy 107 (2016) 78–94, http://dx.doi.org/10.1016/j.energy.2016.03.134.

[17] Q. Shi, J. Lv, C. Guo, B. Zheng, Experimental and simulation analysis of a PV/T system under the pattern of natural circulation, Appl. Therm. Eng. 121 (2017) 828–837, http://dx.doi.org/10.1016/j.applthermaleng.2017.04.140.

[18] J.H. Watmuff, W.W.S. Charters, D. Proctor, Solar and wind induced external coefficients for solar collectors, Comples Intl. Revue Heliotechnique 2 (1977) 56.

[19] F.P. Incropera, D. Dewitt, T.L. Bergman, A.S. Lavine, Fundamentals of Heat and Mass Transfer, 6th ed., John Wiley & Sons, 2007.

[20] S.W. Churchill, H.S. Chu, Correlating equations for laminar and turbulent free convection from a vertical plate, Int. J. Heat Mass Transf. 18 (1975) 1323–1329, http://dx.doi.org/10.1016/0017-9310(75)90243-4.

[21] W.C. Swinbank, Long-wave radiation from clear skies, Q.J. Roy. Meteorol. Soc. 89 (1963) 339–348, http://dx.doi.org/10.1002/qj.49708938105.

[22] P. Berdhal, M. Martin, Emissivity of clear skies, Sol. Energy 32 (1984) 663–664, http://dx.doi.org/10.1016/0038-092X(84)90144-0.

[23] M. Aubinet, Longwave sky radiation parametrizations, Sol. Energy 53 (1994) 147–154, http://dx.doi.org/10.1016/0038-092X(84)90475-8.

[24] V. Gnielinski, On heat transfer in tubes, Int. J. Heat Mass Transf. 63 (2013) 134–140, http://dx.doi.org/10.1016/j.ijheatmasstransfer.2013.04.015.

[25] L. Migliorini, L. Molinaroli, R. Simonetti, G. Manzolini, Development and experimental validation of a comprehensive thermoelectric dynamic model of photovoltaic modules, Sol. Energy 144 (2017) 489–501, http://dx.doi.org/10.1016/j.solener.2017.01.045.

[26] A. Dolara, S. Leva, G. Manzolini, Comparison of different physical models for pv power output prediction, Sol. Energy 119 (2015) 83–99, http://dx.doi.org/10.1016/j.solener.2015.06.017.

[27] W. De Soto, S.A. Klein, W.A. Beckman, Improvement and validation of a model for photovoltaic array performance, Sol. Energy 80 (2006) 78–88, http://dx.doi.org/10.1016/j.solener.2005.06.010.

[28] P. Bombarda, G. Di Marcoberardino, A. Lucchini, S. Leva, G. Manzolini, L. Molinaroli, F. Pedranzini, R. Simonetti, Thermal and electric performances of roll-bond flat plate applied to conventional PV modules for heat recovery, Appl. Therm. Eng 105 (2016) 304–313, http://dx.doi.org/10.1016/j.applthermaleng.2016.05.172.

[29] E. Kaplani, S. Kaplanis, Thermal modelling and experimental assessment of the dependence of PV module temperature on wind velocity and direction, module orientation and inclination, Sol. Energy 107 (2014) 443–460, http://dx.doi.org/10.1016/j.solener.2014.05.037.